New insights in the Photocatalytic Properties of RuO$_2$/TiO$_2$ Mesoporous Heterostructures for Hydrogen Production and Organic Pollutant Photodecomposition.

Md. Tamez Uddin,[1] Odile Babot,[1] Laurent Thomas,[1] Massimiliano D'Arienzo,[2] Franca Morazzoni,[2] Wolfram Jaegermann,[3] Nils Rockstroh,[4] Henrick Junge,[4] Thierry Toupance,[1]*

[1]Univ. Bordeaux, Institut des Sciences Moléculaires, UMR 5255 CNRS, 351 Cours de la Libération, F-33405 Talence Cedex, France.

[2]INSTM, Department of Materials Science, University of Milano-Bicocca, Via R. Cozzi 53, I-20125 Milano, Italy.

[3]Institute of Material Science, Technische Universität Darmstadt, Petersenstrasse 23, D-64287 Darmstadt, Germany.

[3]Leibniz Institute for Catalysis, University of Rostock, Albert-Einstein-Strasse 29a, D-18059 Rostock, Germany.

*Univ. Bordeaux, 351 Cours de la Libération, F-33405 Talence Cedex, France ; Tel: 33 (0)5 40 00 25 23. E-mail: t.toupance@ism.u-bordeaux1.fr

ABSTRACT:

Photocatalytic activities of mesoporous heterostructure RuO_2/TiO_2 nanocomposites for organic dye decomposition and H_2 production by methanol photoreforming have been studied as a function of the RuO_2 loading in the 1-10wt% range. According to Powder X-ray Diffraction, N_2 sorption analyses, Transmission Electron Microscopy and X-ray Photoelectron Spectroscopy, all nanocomposites are made of a mesoporous network of aggregated RuO_2 and TiO_2 nanoparticles, textural properties being almost independent upon the RuO_2 loading. However, an optimum RuO_2 loading has been evidenced for both kinds of reaction, the corresponding nanocomposites showing much higher activities than pure TiO_2 and commercial reference P25. Thus, heterojunction 1 wt% RuO_2/TiO_2 photocatalyst led to the highest rates for the degradation of cationic (methylene blue) and anionic (methyl orange) dyes under UV light illumination. To get a better understanding of the mechanisms involved, a comprehensive investigation on the photogenerated charge carriers, detected by electron spin resonance (ESR) spectroscopy in the form of O^-, Ti^{3+} and O_2^- trapping centers, was performed. Along with the key role of superoxide paramagnetic species in the photodecomposition of organic dyes, ESR measurements revealed a higher amount of trapped holes in the case of the 1wt% RuO_2/TiO_2 photocatalyst that allowed rationalizing the trends observed. On the other hand, a maximum average hydrogen production rate of 618 µmol h^{-1} was reached with heterojunction 5 wt% RuO_2/TiO_2 photocatalyst to be compared with 29 µmol h^{-1} found without RuO_2 that points out the key role of RuO_2 for efficient hydrogen production. Favorable band bending at the RuO_2/TiO_2 interface and the key role of photogenerated holes have been proposed to explain the highest activity of the RuO_2/TiO_2 photocatalysts for hydrogen production. These findings open new avenues for further design of RuO_2/TiO_2 nanostructures with

a fine tuning of the RuO$_2$ nanoparticle distribution in order to reach optimized vectorial charge distribution and enhanced photocatalytic hydrogen production rates.

1. INTRODUCTION

Environmental issues along with the continuous energy demand increase arising from the global population growth require the development of advanced technologies addressed towards the production of green fuels or the efficient elimination of harmful pharmaceutical or organic pollutants. In this context, semiconductor heterogeneous photocatalysis appeared to be a versatile concept for green technology,[1,2] and was directed to a wide range of purposes as hydrogen production, C-C bond formation, carbon dioxide remediation and depollution.[3] So far, titanium dioxide (TiO_2) is the best understood prototype of metal oxide semiconductor for photocatalytic applications due to both fundamental and practical reasons such as good biological and chemical stabilities, low cost, non-toxicity and long-term stability against photocorrosion and chemical corrosion, combined with rather high photocatalytic efficiencies.[4,1] Nevertheless the use of this metal oxide suffers from some limitations related to fast recombination phenomena of photoinduced electron–hole pairs during photocatalytic processes. In this context, different strategies have been investigated to lower the recombination rate of electron-hole pairs by designing metal/metal oxide (Ag/TiO_2[5,6] or Au/TiO_2[7,8]), n-type metal oxide/n-type metal oxide (SnO_2-TiO_2)[9,10] or p-type metal oxide/n-type metal oxide ($NiO-TiO_2$)[11,12] heterostructure nanocatalyts. Such heterojunctions favor charge separation through an easy transfer of electrons or holes from one material to the other depending upon the band alignment at the interface.[13]

Belonging to the family of transition metal oxides with rutile-like structure, ruthenium(IV) oxide (RuO_2) shows an intrinsic submetallic property and its Fermi level EF is situated in the partially filled Ru 4d state.[14,15] Moreover, when TiO_2 is put into contact with RuO_2, that has a high work function[16] situated in the band gap above the valence band of TiO_2, hole transfer from TiO_2 to RuO_2 can be expected after irradiation of the nanocomposite. However, no sufficient attention has

been paid so far concerning the study and the rationalization of the photocatalytic properties of RuO$_2$/TiO$_2$ nanocomposites.[17,18,19,20] We have recently reported a thoroughly study of the band aligment in RuO$_2$/TiO$_2$ nanocomposites which allowed explaining the best photocatalytic properties of this heterojunction compared to pure TiO$_2$.[21] Nevertheless, there have been not any efforts toward the investigation of the RuO$_2$/TiO$_2$ nanocomposites in connection to the type, amount and location of the paramagnetic defects involved in the photocatalytic processes.

Aiming at addressing these points, we report the study of the photocatalytic activity under UV-light of RuO$_2$/TiO$_2$ nanocomposites in two different processes: the photodecomposition of organic dyes and the production of hydrogen by methanol photoreforming. Depending upon the nature of the reaction investigated, an optimum RuO$_2$ loading was determined. To get deeper insight into the photocatalytic mechanism, a comprehensive investigation on the photogenerated charge carriers, detected by electron spin resonance (ESR) spectroscopy in the form of O$^-$, Ti^{3+} and O$_2^-$ trapping centers, was performed. Their abundance were related to the RuO$_2$ loading and to the photoefficiency of the catalysts. This study may represent a first attempt towards an effective detection of the charge trapping centers involved in the photocatalytic reactions assisted by RuO$_2$/TiO$_2$ heterostructures.

2. EXPERIMENTAL METHODS

2.1. Synthesis.

RuO$_2$/TiO$_2$ photocatalytic heterostructures were prepared by impregnation of anatase TiO$_2$ nanopowders[22] with a ruthenium(III) salt according to a previously reported procedure.[21] In a typical synthesis experiment, anatase TiO$_2$ nanopowder (0.3 g) was suspended into a solution of a given amount of ruthenium (III) pentan-2,4-dionate (Alfa Aesar) in tetrahydrofuran (50 mL). After

being stirred at room temperature for 4 h, the volatiles were evaporated and the resulting solids were dried at 70 °C overnight. Further calcination at 400°C in air for 6h yielded the target RuO_2/TiO_2 catalyst. Samples including 1, 2.5, 5 and 10wt% of RuO_2 were synthesized by adding 0.0091, 0.023, 0.047 and 0.094 g of ruthenium (III) pentan-2,4-dionate, respectively, to THF (50 mL). The resulting samples are hereafter named 1wt% RuO_2/TiO_2, 2.5wt% RuO_2/TiO_2, 5wt% RuO_2/TiO_2 and 10wt% RuO_2/TiO_2 nanocomposites.

2.2. Characterization methods

A Bruker AXS diffractometer (D2 PHASER A26-X1-A2B0D3A) including a Cu anode ($K\alpha$ radiation) and a ASAP2010 micromeritric equipment were used to record X-ray diffraction (XRD) patterns and nitrogen adsorption-desorption isotherms respectively, according to previously established procedures.[21,23] X-ray photoelectron spectroscopy experiments were performed at the Darmstadt Integrated System for MATerial research (DAISY-MAT) using previously reported procedures.[24] Transmission Electron Microscopy (TEM) was carried out using a JEOL JEM 2100F (JEOL, Tokyo, Japan) operating at an acceleration voltage of 200 kV (wavelength $\lambda = 2.51pm$) equipped with a Schottky-type FEG and an EDS system (Oxford, Wiesbaden, Germany). For the sample preparation, the photocatalyst powders were dispersed in an ultrasonic bath (high purity methanol 99.8%, Sigma–Aldrich Co.) and a small droplet of the suspension was placed on holey carbon (Cu) grid. ESR investigation was performed by a Bruker EMX spectrometer operating at the X-band frequency and equipped with an Oxford cryostat working in the temperature range of 4-298 K. The nanocrystals were charged into quartz glass tubes connected both to a high vacuum pumping system and to a controlled gas feed (O_2). Spectra were recorded at 130 K in vacuo conditions ($p < 10^{-5}$ mbar), before and after 30 min of UV irradiation inside the ESR cavity either in vacuo ($p < 10^{-5}$ mbar) or in the presence of $p(O_2) = 10$ mbar. For each sample, the

absence of a signal before irradiation was checked. No significant differences resulted between the spectra recorded just before and 20 min after switching off the UV irradiation, except a small decrease of the signal intensity. Spectra were acquired with a modulation frequency of 100 kHz, modulation amplitudes of 5 gauss, and microwave powers of 10 mW. Irradiation was performed by an UV 150 W Xe lamp (Oriel) with the output radiation focused on the samples in the cavity by an optical fiber (50 cm length, 0.3 cm diameter). The g values were calculated by standardization with α,α' - diphenyl - β - picryl hydrazyl (DPPH). The spin concentration was obtained by double integration of the resonance lines, referring to the area of the standard Bruker weak pitch ($9.7 \times 10^{12} \pm 5\%$ spins cm^{-1}). Accuracy on double integration was $\pm 15\%$. Care was taken to always keep the most sensitive part of the ESR cavity (1 cm length) filled. Spectra simulations and fits were performed using the SIM 32 program.[25]

2.3. Photocatalytic experiment

Photocatalytic activity of the different nanocatalysts was first examined by the degradation of methyl orange (MO) dye (Alfa Aesar, reagent grade, used as supplied) under UV-light. All the experiments were conducted at room temperature in a Pyrex beaker open to air illuminated with a 125 W high pressure mercury lamp (Philips, HPL-N 125 W/542 E27), emitting UV light, positioned above the solution beaker. In a typical experiment, 0.1 g of photocatalyst was immersed in 100 mL of MO aqueous solution (10 mg/L) that corresponds of a catalyst concentration of 1.0 g/L. Prior to irradiation, the suspension was stirred in the dark for 30 min to reach adsorption/desorption equilibrium. Small amounts of dye solution were withdrawn firstly after dark stirring and afterward in regular time intervals from the reactor and then centrifuged (4000 rpm, 10 min). Monitoring the absorption intensity of MO at 464 nm with a UV-Visible Spectrophotometer (Shimadzu, UV-1650 pc) led to the remaining amount of dyes. In all the cases,

blank experiments were also conducted with the catalysts in the absence of light and without the catalysts when the solution containing the dissolved dye was illuminated.

Furthermore, the photocatalytic production of hydrogen (H_2) was carried out in an argon atmosphere and under exclusion of air. Solvents were distilled under an argon atmosphere, or degassed via standard procedures prior to use and stored under argon. The UV light source a was Hg vapor light source (LUMATEC SUPERLITE 400) emitting in the 320-400 nm wavelength range with an input power of 1.6 W. Each photocatalytic experiment was conducted in a double walled thermostatically controlled reaction vessel (at a constant temperature of 25.0°C) which was connected via a condenser to an automatic gas burette. In a typical reaction, the double-walled reaction vessel connected to the automatic gas burette was evacuated and flushed with argon three times to remove any other gases. The photocatalysts were introduced as a powder and the mixture of methanol/H_2O (1:1, 10 mL) was added, and the temperature was maintained at 25°C by a thermostat. The mixture was stirred (300 rpm) for 5 min to reach thermal equilibrium. The photocatalytic reaction was started by irradiating the reaction vessel with light. The volumes of the evolved gases were determined by an automatic gas burette. The gas burette was equipped with to a pressure sensor. Evolving gas during the reaction causes a pressure increase in the closed system, which is compensated by volume increase of the burette syringe by an automatic controlling unit. The gas evolution curves are collected by a PC. After each reaction a gas sample was taken and quantitatively analyzed by gas chromatography (HP6890N, carboxen 1000, thermal conductivity detector (TCD) and methanizer/flame ionization detector (FID), external calibration). The variance of the volumes for reproduction of experiments was between 1–15%.

3. RESULTS AND DISCUSSION

3.1. Characterization of nanocatalysts

The XRD patterns of TiO_2 and heterostructure RuO_2/TiO_2 nanocatalysts containing different wt % (1.0, 5.0, and 10.0) of RuO_2 exhibited the diffraction lines expected for anatase TiO_2 (JCPDS 21-1272), traces of brookite TiO_2 (JCPDS 29-1360) and rutile RuO_2 (JCPDS 43-1027). As shown in Figure 1, the intensity of the peaks at 28.1 and 35.5 2θ, which are attributed to RuO_2 (110) and (101) planes, increased with the amount of RuO_2 introduced.
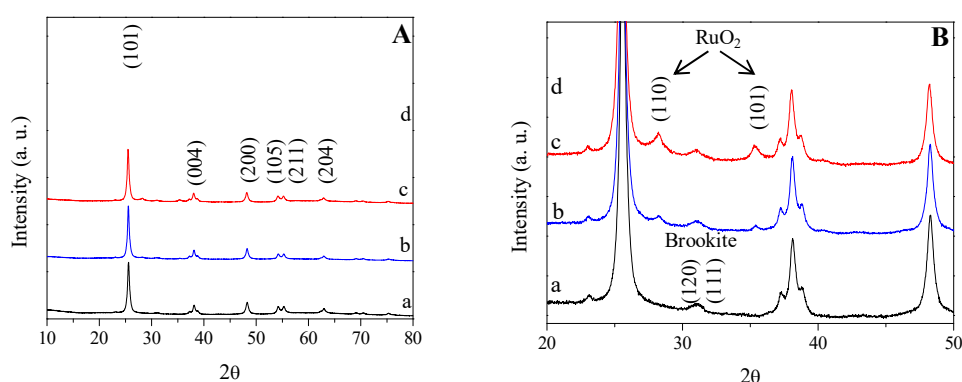
Figure 1. XRD of TiO_2 (a, black), 1wt% RuO_2/TiO_2 (b, blue), 5wt% RuO_2/TiO_2 (c, red) and 10wt% RuO_2/TiO_2 (d, olive) nanomaterials: **A**: 2θ region of 10-80°. **B**: Higher magnification of the 2θ region of 20-50°.

As far as the textural properties are concerned, each sample showed a typical type IV N_2 adsorption-desorption isotherm including a hysteresis loop which is typical of mesoporous materials, according to the IUPAC classification, as depicted in Figure 2.[26] Increasing the RuO_2 content induced a slight decrease of the specific surface area (S_{BET}) that was found to be 68, 67, 69, 63 and 60 ± 2 m^2g^{-1} for TiO_2, 1wt% RuO_2/TiO_2, 2.5wt% RuO_2/TiO_2, 5wt% RuO_2/TiO_2 and 10wt% RuO_2/TiO_2, respectively. Moreover, the presence of a hysteresis loop indicates that each sample contained pores of non-uniform size and shapes that is characteristic of solids consisting of particles crossed by nearly cylindrical channels or made by aggregates (consolidated) or

agglomerates (unconsolidated) of spheroidal particles.[27] It is also worth mentioning that the pore size distribution was found to be similar whatever the RuO_2 loading that suggests that the mesoporosity does not depend upon the RuO_2 amount in the 1-10 wt% range (Figure 2, inset). The materials synthesized can be therefore seen as a nanocrystalline mesoporous photocatalysts made of anatase TiO_2 and rutile RuO_2 nanocrystallites.
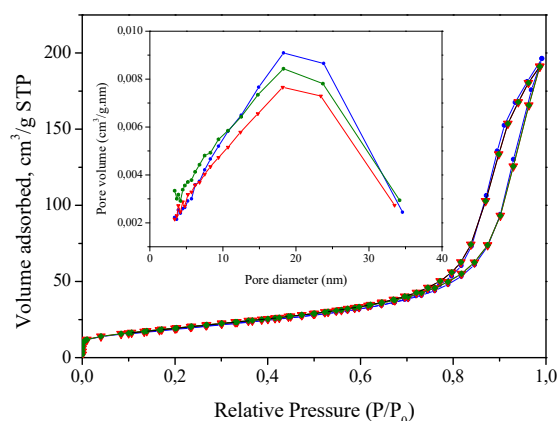

Figure 2. Nitrogen gas adsorption-desorption isotherms and pore-size distribution (inset) of 1wt% (circle, blue), 5wt% (down triangle, red) and 10 wt% (diamond, olive) RuO_2/TiO_2 photocatalysts.

To confirm the deposition of RuO_2 on the surface of TiO_2, scanning transmission electron (STEM) bright field (BF) and high angle annular dark field (HAADF) experiments were performed. First of all, the TEM image of RuO_2/TiO_2 sample containing 5 wt% RuO_2 was measured. It can be seen that the RuO_2 is deposited as cluster (can you tell the dimensions? So that we can be sure if they are cluster or not) on the surface of TiO_2 nanoparticles (Figure 3A). The BF image (Figure 3B) showed the presence of RuO_2 nanoparticles with a clear contrast in STEM-HAADF image (Figure 3C) indicating the deposition of RuO_2 on TiO_2 surface. Contrast variation was observed between RuO_2 and TiO_2 nanoparticles, because the contrast variation in STEM images is Z-related and due to the higher atomic number of Ru, those particles are brighter in

HAADF images. EDX analysis performed on the sample (Figure 3E) further confirmed the presence of RuO_2 deposited on the surface of TiO_2.
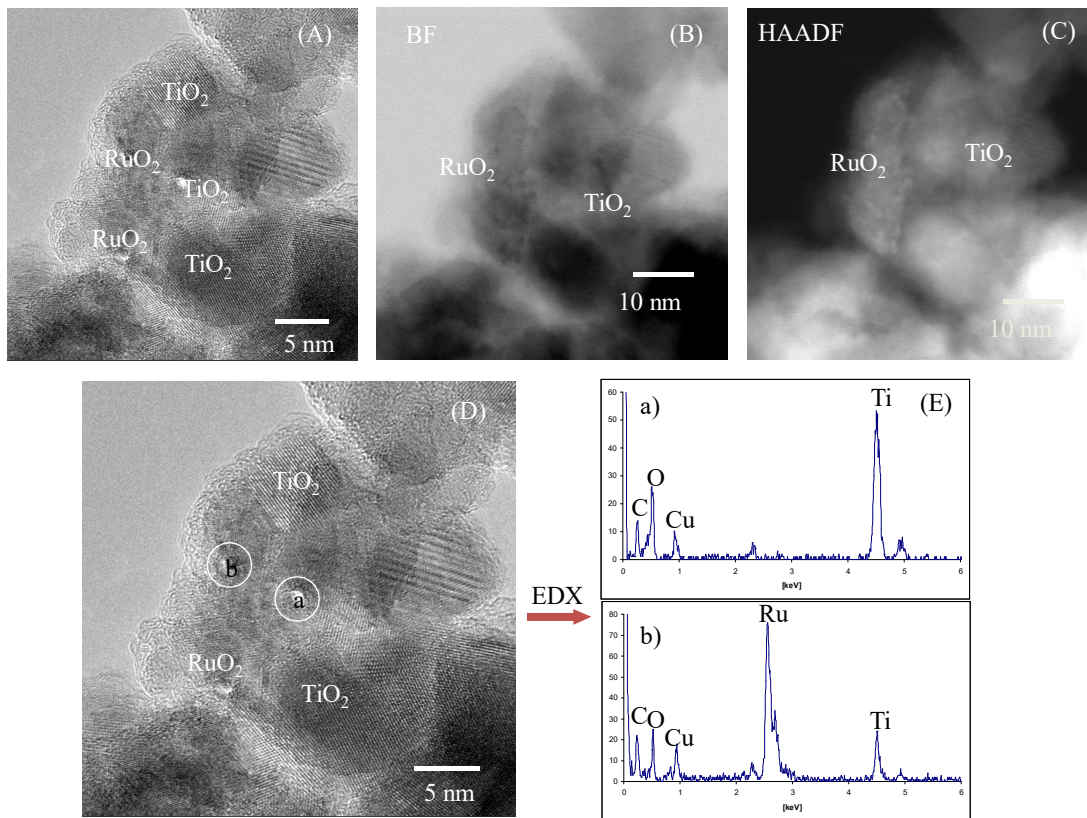

Figure 3. A: (A) TEM (B) STEM-BF (C) STEM-HAADF images and (D, E) EDX mapping of 5 wt% RuO_2/TiO_2 nanoparticles.

Finally the surface composition of the RuO_2/TiO_2 nanocomposites was studied by X-ray photoelectron spectroscopy. As previously found for the 1wt% RuO_2/TiO_2 sample,[21] only the characteristic features of titanium, oxygen and ruthenium, along with those of adventitious carbon species, were observed in the spectra of the 5wt% RuO_2/TiO_2 and 10wt% RuO_2/TiO_2 samples (Figures 4 and Figure S1). The presence of ruthenium was clearly evidenced by the detection of the Ru $3d_{5/2}$ emission line located at 280.55 eV which is typical of Ru^{4+} cations as expected for RuO_2 (Figure 4B).[28] The high-resolution XPS spectra for Ti 2p yielded binding energies of 464.4 and 458.7 eV assigned to Ti $2p_{1/2}$ and Ti $2p_{3/2}$ core levels, respectively (Figure 4C). The spin-orbit

splitting was found to be 5.7 eV which is in good agreement with the one expected for Ti^{4+} oxidation state in TiO_2-based nanocomposites.[29] Moreover, no evidence of Ti^{3+} could be found in the spectrum. Finally, the main component of the O1s peak located at 530.5 eV was attributed to O-Ti bonds in bulk TiO_2, whereas the tailing to higher energies can be related to hydroxylation of TiO_2 particles (Figure 4D). As a result, both 5wt% RuO_2/TiO_2 and 10wt% RuO_2/TiO_2 nanocomposites are made of RuO_2 and TiO_2 nanoparticles.

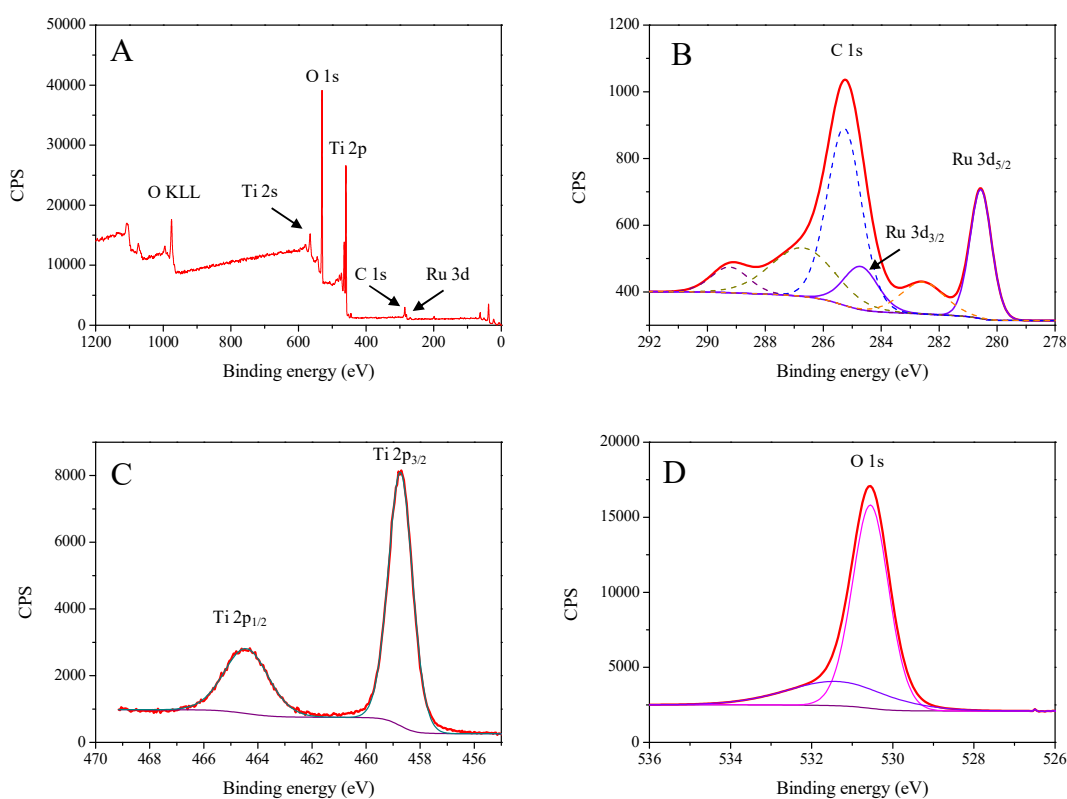**Figure 4.** A) XPS Survey spectrum for 5wt% RuO_2/TiO_2 nanocomposite; B) High resolution XPS spectrum of C 1s + Ru 3d after deconvolution for 5wt% RuO_2/TiO_2 nanocomposite; C) High resolution XPS spectrum of Ti 2p for 5wt% RuO_2/TiO_2 nanocomposite; D) High resolution XPS spectrum of O 1s after deconvolution for 5wt% RuO_2/TiO_2 nanocomposite;.

3.2. Photocatalytic activity

To complete our previous study concerning on the photocatalytic decomposition of cationic dyes (methylene blue (MB)) with catalytic amounts of RuO_2/TiO_2 nanomaterials,[21] similar experiments were performed with methyl orange (MO) as a typical anionic dye.[30] While MO remained stable under UV irradiation without any catalyst, a progressive decrease in absorption 464 nm along with a slight shift of the bands toward shorter wavelengths were detected upon addition of the nanocatalyst (Figure 5A). Furthermore, the photodegradation of MO by RuO_2/TiO_2 heterojunction nanocatalysts follows a first- order law, $\ln(C/C_0) = - k_{app}t$, where k_{app} is the pseudo first-order rate constant (Figure 5B, Table 1). As for MB,[21] 1wt% RuO_2/TiO_2 nanocatalyst showed the highest photocatalytic activity in the photocatalytic decomposition of MO with an apparent degradation rate constant reaching 0.065 min^{-1}, value 2 times higher than those obtained with commercial TiO_2 P25, respectively.
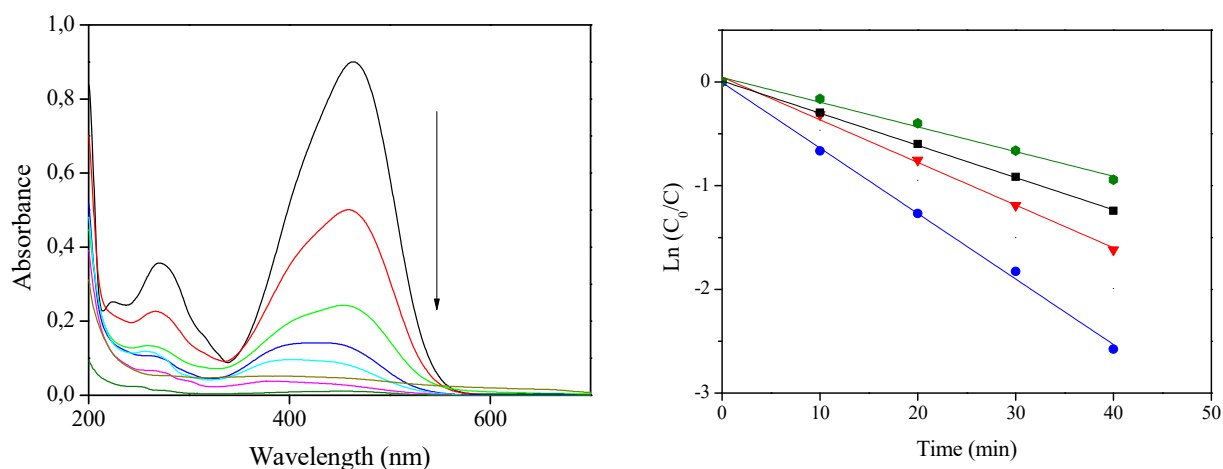

Figure 5. (**left**) Absorbance changes of MO solution after different irradiation times in the presence of the 1wt% RuO_2/TiO_2 sample: equilibrium (black), 10 min (red), 20 min (green), 30 min (blur), 40 min (cyan), 50 min (dark yellow), 60 min (magenta) and 80 min (olive). (**right**) $\ln[C/C_0]$ as a function of the irradiation time for TiO_2 (square, black), 1wt% RuO_2/TiO_2 (circle, blue), 5wt% RuO_2/TiO_2 (down triangle, red) and 10 wt% RuO_2/TiO_2 (diamond, olive) photocatalysts

Table 1. Apparent rate constants for the degradation of MO[a] and MB[b] of TiO_2, P25 and RuO_2/TiO_2 nanocatalysts.

Photocatalyst	TiO_2	1% RuO_2/TiO_2	2.5% RuO_2/TiO_2	5% RuO_2/TiO_2	10% RuO_2/TiO_2	P25
k_{app} MO (min^{-1})	0.032	0.065	0.049	0.039	0.023	0.033
k_{app} MB (min^{-1})	0.101	0.239	0.192	0.165	0.081	0.101

[a] This study. [b]According to reference 21.

The photocatalytic activity of the various heterostructures was also determined in the hydrogen (H_2) evolution from methanol steam reforming reaction (Figure 6). As evidenced in Figure 6A, the H_2 production after 3 h under UV irradiation was only 20.4 mL without photocatalysts, whereas in the absence of methanol but in the presence of catalysts, the evolved H_2 resulted 24.5 mL. In contrast, the H_2 production was increased more than 77 times in the presence of photocatalyst (5 wt% RuO_2/TiO_2) and methanol. These results revealed that both photocatalysts and sacrificial agent are required for an effective photocatalytic H_2 production. The time-course of the photocatalytic gas evolution over TiO_2 and RuO_2/TiO_2 containing different amount of RuO_2 is shown in Figure 6B. The amount of the evolved gas almost linearly increased with increasing irradiation time. The gas mixture mainly contained H_2 along with a small amount of carbon dioxide (CO_2), in an amount of 0.31 wt%, but without any oxygen (O_2) and methane (CH_4) traces. As far as the hydrogen production is concerned (Figure 6C), the yield of H_2 over heterostructure RuO_2/TiO_2 photocatalysts was higher than that obtained over pure TiO_2 and commercial TiO_2 P25, whatever the RuO_2 content. As a consequence, the presence of RuO_2 played a key role in photocatalytic H_2 production. To get a deeper insight in this issue, the influence of the RuO_2 loading on the photocatalytic H_2 production was studied (Figure 6D). It can be clearly seen that

the rate of H_2 production increased initially by increasing the RuO_2 content, reached a maximum and then started to decrease once the RuO_2 content reached a certain value. Increasing the RuO_2 content from 1 wt% to 5 wt%, the H_2 production rate increased from 441µmol/h to 618 µmol/h, the 5 wt% RuO_2/TiO_2 nanocatalyst yielding the highest rate of H_2 production. In contrast, with further increase in RuO_2 content from 5 wt% to 10 wt%, the H_2 production rate dropped rapidly from 618 µmol/h to 353 µmol/h.
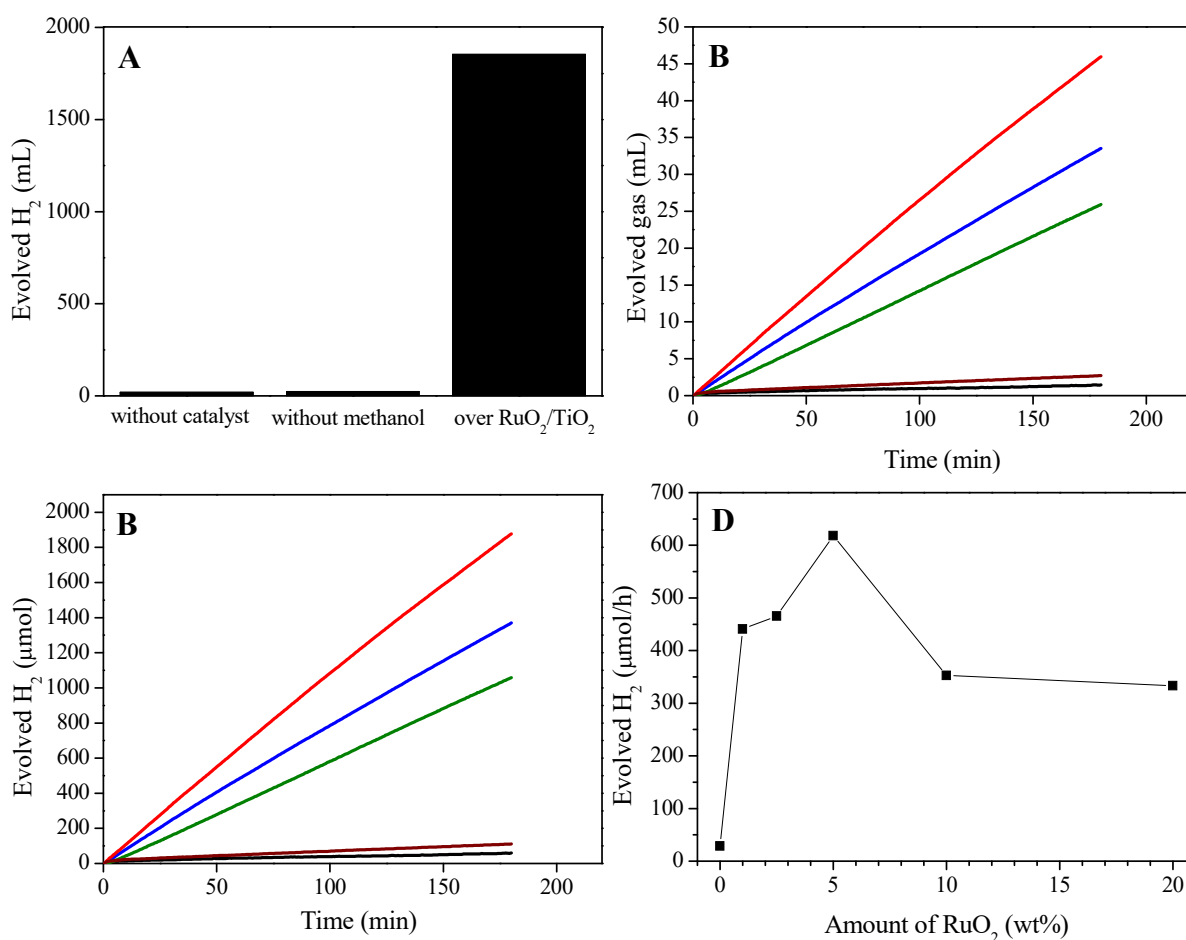

Figure 6. (A) photocatalytic evolution of H_2 under different condition, photocatalytic evolution of gas (B) and H_2 (C) over TiO_2 (black), P25 (wine), 1 wt% RuO_2/TiO_2 (blue), 5 wt% RuO_2/TiO_2 (red) and 10 wt% RuO_2/TiO_2 (olive) photocatalysts and (D) effect of RuO_2 loading on the H_2 production. All the experiments were run for 3 h under identical conditions.

3.3. Mechanistic investigations

Introduction of RuO_2 clearly enhanced the photocatalytic properties of TiO_2 for both photodecomposition of organic dye and hydrogen production. As the textural properties (S_{BET} and mesoporosity) of all the nanocomposites studied are similar, the effect is related to better charge separation, as a consequence of suitable band alignment previously shown by our UPS/XPS studies.[21] However, the optimum RuO_2 content strongly depends on the kind of photocatalytic reaction envisaged, values of 1wt% and 5 wt% having been determined for organic dye degradation and hydrogen production, respectively.

As a consequence, in order to study how the doping with RuO_2 affects the formation of the charge trapping centers upon UV excitation and, in turn, the photocatalytic activity of TiO_2, 1wt% RuO_2/TiO_2, 2.5wt% RuO_2/TiO_2 and 5wt% RuO_2/TiO_2 nanocatalysts, ESR investigation was performed after UV irradiation at 130 K, either in vacuo ($p < 10^{-5}$ mbar) or in the presence of p $(O_2) = 10$ mbar. After irradiation under vacuum, pure TiO_2 nanocatalysts (TiO_2, Figure 7a), show broad and weak resonances at g = 1.976, attributable to Ti^{3+} centers (Ti^{3+}[II] species).[31] No Ti^{3+} species are instead detectable in 1wt% RuO_2/TiO_2 anatase nanocrystals (Figure 7b) Increasing the percentage of RuO_2 (2.5wt% RuO_2/TiO_2, Figure 7c), the spectrum displays the presence of higher field features assigned to electrons trapped at two different Ti^{3+}centers: species [I], attributable to Ti^{3+} centers in a ordered crystalline environment and species [II], broader and weaker, ascribable to Ti^{3+}centers located in a disordered environment and probably near to the surface.[31] The g values of these species are reported in Table 2. At highest Ru concentration (2.5wt% RuO_2/TiO_2, Figure 7d), Ti^{3+} species are no more attribuable.

The intense resonances at lower fields (Figure 7), can be attributed to coexisting oxygen species, O^- and O_2^-,[32,33] whose g values and relative contributions have been calculated by signal simulation (Table 2). In particular, Figure 8 reports the the deconvolutions of the EPR signals of 1wt%

RuO$_2$/TiO$_2$ (Figure 8a) and 2.5wt% RuO$_2$/TiO$_2$ (Figure 8b) samples. The presence of O$_2^-$ species, mainly occurring in 2.5wt% RuO$_2$/TiO$_2$ nanocrystals, even when UV irradiation was performed under vacuum, may be related to the evolution of residuals OH$^-$ groups according to the following mechanism:[34]
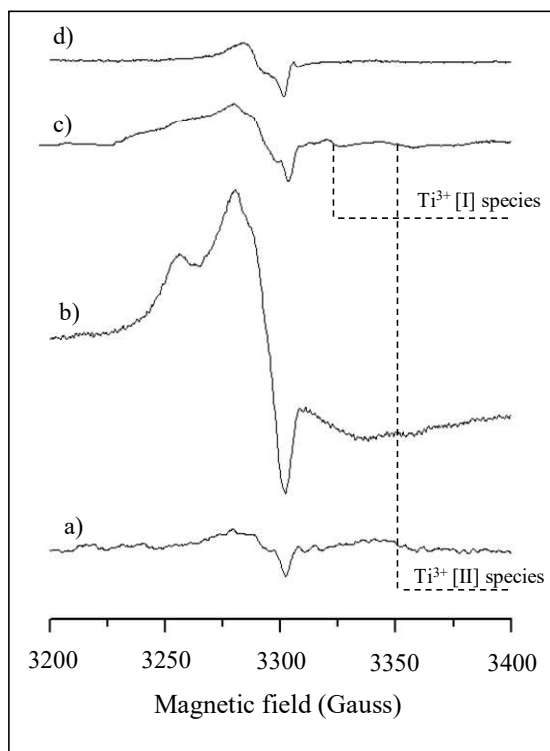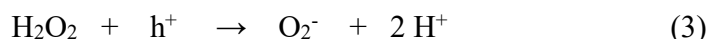
$$h^+ \; + \; OH^- \; \rightarrow \; {}^{\bullet}OH \qquad\qquad (1)$$

$$2\,{}^{\bullet}OH \; \rightarrow \; H_2O_2 \qquad\qquad (2)$$

$$H_2O_2 \; + \; h^+ \; \rightarrow \; O_2^- \; + \; 2\,H^+ \qquad\qquad (3)$$

$$O_2^- \; + \; h^+ \; \rightarrow \; O_2 \qquad\qquad (4)$$

Figure 7. Experimental ESR spectra at 130 K after UV irradiation in vacuum (p < 10^{-5} mbar) of: a) TiO$_2$, b) 1wt% RuO$_2$/TiO$_2$, c) 2.5wt% RuO$_2$/TiO$_2$ and d) 5wt% RuO$_2$/TiO$_2$ nanocrystals. Dashed lines highlight the signals attributed to Ti^{3+} species.

Considering their determinant role in oxidative catalysis (see below), the relative contribution of the O^- species (calculated as % of the total intensity of the $O^- + O_2^-$ signals) was determined and reported in Table 2, for the different samples.

Table 2. *g* tensor values of the paramagnetic defects detected after photoexcitation in vacuum ($p < 10^{-5}$ mbar) in TiO_2 and TiO_2/RuO_2 nanocrystals, determined by simulation of the ESR features. The relative contribution of the O^- species (calculated as % of the total intensity of the $O^- + O_2^-$ signals) is also reported.

Photocatalyst	O^- centers (%)	O^- species	Ti^{3+} species	O_2^- species
TiO_2	100%	$g\perp = 2.0129$, $g\| = 2.0047$	$g\perp \sim 1.976$ $g\| =$ n.d.	/
1% RuO_2-TiO_2	50%	$g\perp = 2.0100$, $g\| = 2.0028$	/	$g_{zz} = 2.0286$, $g_{yy} = 2.0096$, $g_{xx} = 2.0003$
2.5% RuO_2-TiO_2	27%	$g\perp = 2.0129$, $g\| = 2.0036$	Ti^{3+}[I]: $g\perp = 1.9880$ $g\| =$ n.d. Ti^{3+}[II]: $g\perp \sim 1.976$ $g\| =$ n.d.	O_2^-[I]: $g_{zz} = 2.0258$, $g_{yy} = 2.0110$, $g_{xx} = 1.9999$ O_2^-[II]: $g_{zz} = 2.0339$, $g_{yy} = 2.0099$, $g_{xx} = 2.0000$
5% RuO_2-TiO_2	60%	$g\perp = 2.0129$, $g\| = 2.0047$	n.d.	/

The abundance and the stability of the paramagnetic centers detected by ESR after UV irradiation is relatable to the charge separation and to their inhibited recombination.[31,32,33,35] Hence, as already suggested in our previous studies,[31,35] the amount of hole trapping centers can be associated to the efficiency of the photocatalytic processes.
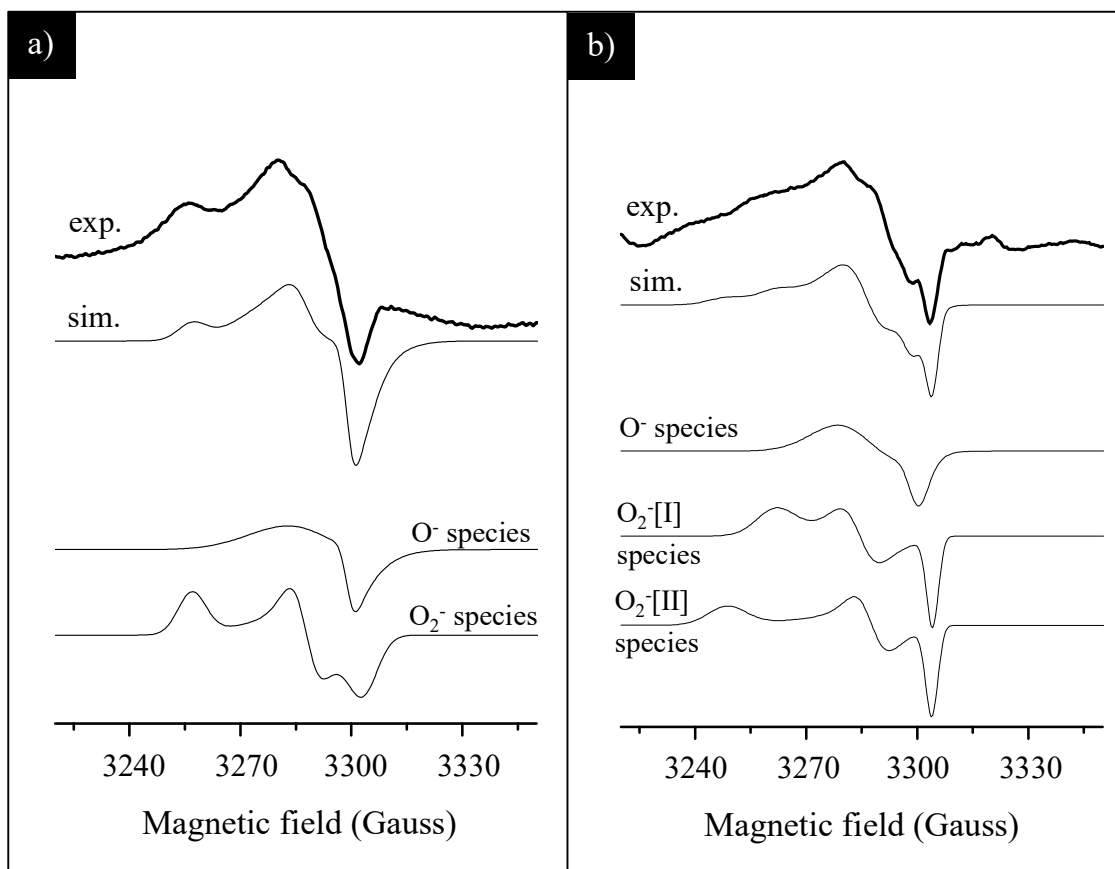
Figure 8. a) Deconvolution (sim.) of ESR signals of 1wt% RuO_2/TiO_2 nanoparticles (exp.) into O^- and O_2^- species; b) Deconvolution (sim.) of ESR signals of 2,5wt% RuO_2/TiO_2 nanoparticles (exp.) into O^- and O_2^- species.

In the present case, from the area of integrated signals obtained after photoexcitation in vacuum, the concentration of holes trapped on O^- centres always exceeds that of electron trapped on Ti^{3+} centres. In particular, when plotted against the apparent reaction rate constant (k_{app}) for the degradation of MB and of MO,[21] the amount of O^- centers increases with the k_{app} increase, i.e. with the increase of photoefficiency (Figure 9), becoming the highest for 1wt% RuO_2/TiO_2. This trend suggests a parallelism between the photoactivity of nanocrystals and the amount of trapped holes which ultimately drives the surface photooxidation processes. On the contrary, considering also

their low amount, no simple relation between the abundance of Ti^{3+} centers and the photoactivity can be suggested.
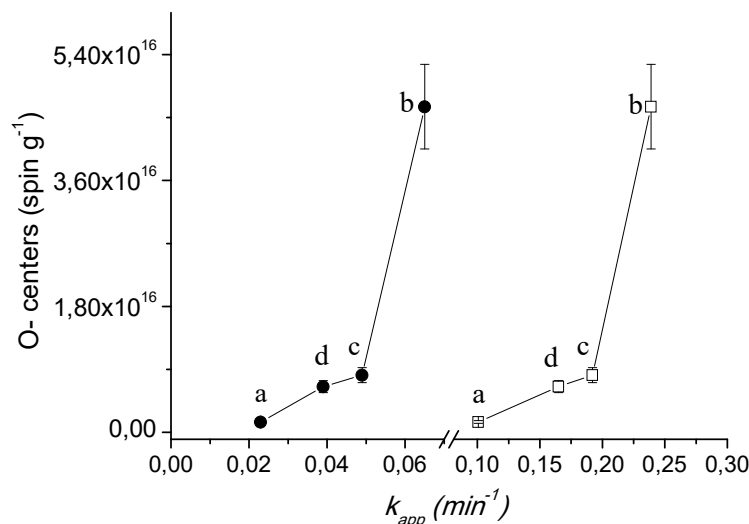

Figure 9. Trend of the relative amounts of O^- species calculated for different nanocatalysts vs. apparent reaction rate constant (k_{app}) for the degradation of MB ($\square$) and MO ($\bullet$). a: TiO_2; b: 1wt% RuO_2/TiO_2; c: 2.5wt% RuO_2/TiO_2; d: 5wt% RuO_2/TiO_2

These outcomes support the idea that the formation of TiO_2/RuO_2 heterojunctions promotes a more efficient electron-hole separation which results, in turn, in an increase of the photocatalytic activity. However, it is also worth mentioning that the photoefficiency in the MB or MO degradation gradually decreased with increasing RuO_2 concentration (k_{app} 5wt% $RuO_2/TiO_2 < k_{app}$ 2.5wt% $RuO_2/TiO_2 < k_{app}$ 1wt% RuO_2/TiO_2). This behavior may be attributed to the possible action of RuO_2 as charge recombination center, when deposited in higher amount on titania.[19] As it has been previously reported that the conductivity of TiO_2/RuO_2 heterostructures is higher than that of bare TiO_2, a more rapid charge transfer and recombination in RuO_2 can be suggested.[36]

In order to further elucidate the mechanism of the MB and MO photooxidative processes, ESR investigations on TiO_2, 1wt% RuO_2/TiO_2, 2.5wt% RuO_2/TiO_2, and 5wt% RuO_2/TiO_2 nanocrystals

were performed after UV irradiation at 130 K in the presence of p (O_2) = 10 mbar and subsequent removal of the residual oxygen by evacuation at p < 10^{-5} mbar.
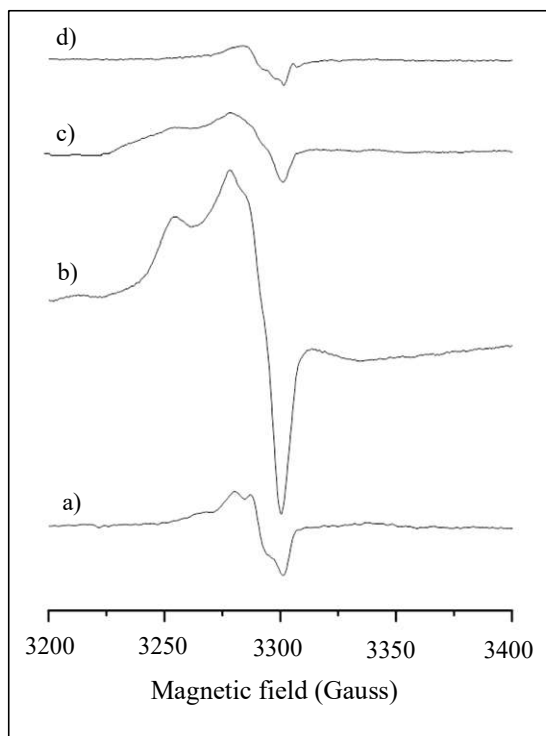

Figure 10. ESR spectra at 130 K after UV irradiation in the presence of 10 mbar of O_2 and then vacuum at p < 10^{-5} mbar of: a) TiO_2, b) 1wt% RuO_2/TiO_2 c) 2.5wt% RuO_2/TiO_2 and d) 5wt% RuO_2/TiO_2 nanocatalysts.

After the oxygen contact (Figure 10), the resonances of O_2^- centers can be easily detected. In particular, it can be observed that the amount of superoxide species formed is higher in 1wt% RuO_2/TiO_2, 2.5wt% RuO_2/TiO_2 and 5wt% RuO_2/TiO_2 than in bare TiO_2 nanoparticles and raises as the k_{app} for the degradation of MB and MO increases (Figure 11). This trend on one hand indicates an indirect involvement of these paramagnetic species in the photooxidative processes, on the other confirms that the creation of TiO_2/RuO_2 heterojunctions effectively improves the charge separation boosting the photoefficiency of RuO_2 doped nanocrystals.
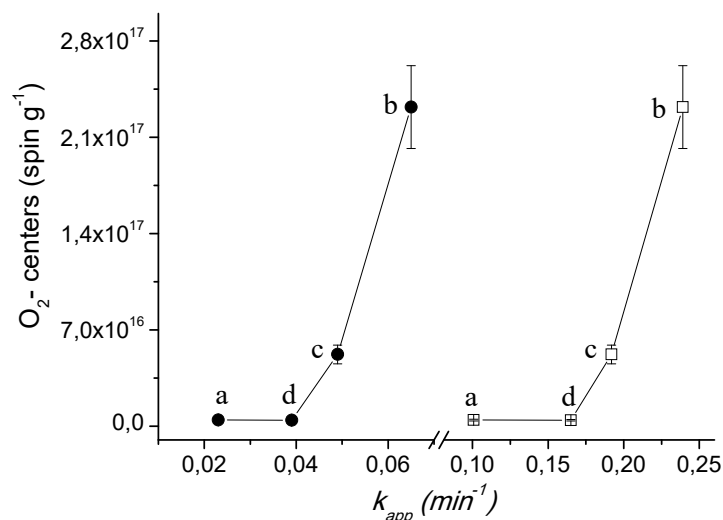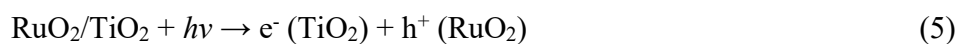
Figure 11. Trend of the abundance of superoxide species (O_2^-) as a function of apparent reaction rate constant (k_{app}) for the degradation of MB ($\square$) and MO ($\bullet$). a) TiO_2, b) 1wt% RuO_2/TiO_2, c) 2.5wt% RuO_2/TiO_2 and d) 5wt% RuO_2/TiO_2 nanocatalysts.

As far as the hydrogen production by methanol photoreforming with these nanocomposites is concerned, the experimental conditions used suggest the following mechanism for H_2 generation. In the absence of oxygen and presence of sacrificial species such as methanol, the holes generated by the light (Eq. (5)) react with methanol (CH_3OH) to produce $^\bullet CH_2OH$ radical. The $^\bullet CH_2OH$ radical possesses sufficiently negative oxidation potential (-0.74 V) and could further react to produce H^+, electron and HCHO ((Eq. (6)).[37] On the other hand, electrons in the conduction band of the particle will simultaneously reduce water or protons in the solution to form gaseous H_2 as shown by Eq. (7). These reactions proceed competitively with the recombination of the photoinduced electrons and holes.
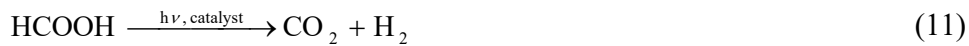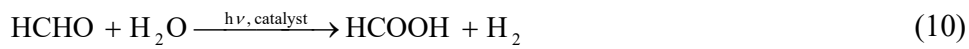
$$RuO_2/TiO_2 + h\nu \rightarrow e^- (TiO_2) + h^+ (RuO_2) \tag{5}$$

$$H^+ + CH_3OH \rightarrow {}^\bullet CH_2OH + H^+ \tag{6}$$

$$\cdot CH_2OH \rightarrow HCHO + H^+ + e^- \tag{7}$$

$$2H_2O + 2e^- \rightarrow H_2 + 2OH^- \tag{8}$$

As a result, the overall reaction is

$$CH_3OH \xrightarrow{h\nu, \, catalyst} HCHO + H_2 \tag{9}$$

Formaldehyde (HCHO) obtained can be further oxidized to methanoic acid HCOOH and subsequently to CO_2 along with hydrogen generation according to:

$$HCHO + H_2O \xrightarrow{h\nu, \, catalyst} HCOOH + H_2 \tag{10}$$

$$HCOOH \xrightarrow{h\nu, \, catalyst} CO_2 + H_2 \tag{11}$$

This mechanism points out the pivotal role h^+ species in enhancing the photo-oxidation of methanol and, consequently, the hydrogen production. As assessed by ESR investigation after photoexcitation in vacuum, the amount of hole traps, i.e. O^- centers, is higher for RuO_2/TiO_2 nanocatalysts than for pure TiO_2. This highlights the role of RuO_2 in stabilizing the photogenerated holes and explains the better ability of the heterojunctions in the hydrogen production. A second key factor favoring H_2 production with RuO_2/TiO_2 nanocatalysts is the Schottky barriers developed at the interface between RuO_2 and TiO_2. Thus, postulating an idealized mechanistic scheme of electron-hole pair separation of a well-defined planar metal-semiconductor contact, our previous XPS studies clearly showed a favorable upward band bending at the interface of RuO_2/TiO_2 heterojunction, the phenomenon increasing with the RuO_2 amount.[21] As a result, the enhanced H_2 production rate with increasing the RuO_2 loading up to 5 wt% can be due to a higher number of Schottky barriers at the RuO_2/TiO_2 interfaces. However, above a certain RuO_2 amount, the active sites on the TiO_2 surface that were available for absorption of light and electron donors can be covered by excessive RuO_2 particles inhibiting the photocatalytic processes. Moreover, as mentioned above, RuO_2 nanoparticles in composites containing higher RuO_2 loadings may act as

recombination centres for photogenerated electrons and holes. Both phenomena are likely at the origin of the significant decrease in photocatalytic activity for RuO_2 loadings higher than 5 wt%.

At this stage, it is worth underlining that changes in morphology and size dependent electronic properties should also be taken into account to rationalize the photocatalytic properties on the basis of band bending at the RuO_2/TiO_2 interface. Indeed, our previous studies showed that the observed band bending in the RuO_2/TiO_2 nanocatalysts is smaller than in a well-defined planar metal-semiconductor contact. Indeed, the small sizes of both TiO_2 and RuO_2 particles does not allow to saturate the band bending as the standard space charge layers thickness will exceed the size of the particles (an effect which depend on doping). Furthermore, the spatial distribution of the RuO_2 deposits on the TiO_2 substrates are not yet optimized, high RuO_2 loading hampering a favorable vectorial charge separation. As a consequence, further efforts are required to control better the RuO_2 nanoparticules distribution over TiO_2 in order to produce highly efficient RuO_2/TiO_2 heterostructures.

4. Conclusion

In summary, mesoporous heterostructure RuO_2/TiO_2 nanoparticles photocatalysts showed enhanced photocatalytic activity in organic dye decomposition and H_2 production by methanol photoreforming compared to pure TiO_2 and commercial P25. For both kinds of photocatalytic reactions, different optimum RuO_2 loading have been evidenced. Thus, heterojunction 1 wt% RuO_2/TiO_2 photocatalyst showed the highest rates for the degradation of MB and MO dyes under UV light irradiation. These findings were rationalized on the basis of ESR studies that evidenced the higher amount of trapped holes for the 1wt% RuO_2/TiO_2 photocatalyst and the role of superoxide paramagnetic species in the photodecomposition of organic dyes. On the other hand,

heterojunction 5 wt% RuO_2/TiO_2 photocatalysts showed the highest catalytic activity with average hydrogen production rate of 618 $\mu mol\ h^{-1}$, the latter decreasing dramatically to 29 $\mu mol\ h^{-1}$ without RuO_2 that points out the key role of RuO_2 for efficient hydrogen production. Favorable band bending at the RuO_2/TiO_2 interface and key role of photogenerated holes have been underlined to explain the highest activity of the RuO_2/TiO_2 photocatalysts for hydrogen production. Further efforts are currently in progress to achieve a better control of the RuO_2 nanoparticle distribution in order to reach optimum vectorial charge distribution and enhanced photocatalytic hydrogen production rates. The overall results support that understanding how the cooperative interaction between RuO_2 and TiO_2 affects the formation and reactivity of charge trapping centers, may lay the groundwork for the development of highly active photocatalysts.

Supporting Information.

SYNOPSIS (TOC)

References

(1) Hoffmann, M. R.; Martin, S. T.; Choi, W.; Bahnemann, D.W. Environmental Applications of Semiconductor Photocatalysis. *Chem. Rev.* **1995**, *95*, 69-96.

(2) Ravelli, D.; Dondi, D.; Fagnoni, M.; Albini, A. Photocatalysis. A Multi-Faceted Concept for Green Chemistry. *Chem. Soc. Rev.* **2009**, *38*, 1999-2011.

(3) Yu, C.; Li, G.; Kumar, S.; Yang, K.; Jin, R. Phase Transformation Synthesis of Novel Ag_2O/Ag_2CO_3 Heterostructures with High Visible Light Efficiency in Photocatalytic Degradation of Pollutants. *Adv. Mater.* **2014**, *26*, 892-898.

(4) Fujishima, A.; Rao, T. N.; Tryk, D. A. Titanium Dioxide Photocatalysis. *J. Photochem. Photobiol. C Photochem.* **2000**, *1*, 1-21.

(5) Logar, M.; Jancar, B.; Sturm, S.; Suvorov, D. Weak Polyion Multilayer-Assisted in situ Synthesis as a Route Toward a Plasmonic Ag/TiO_2 Photocatalyst. *Langmuir* **2010**, *26*, 12215-12224.

(6) Zhang, X.; Zhou, M.; Lei, L. Preparation of an $Ag-TiO_2$ Photocatalyst Coated on Activated Carbon by MOCVD. *Mater. Chem. Phys.* **2005**, *91*, 73-79.

(7) Chen, X.; Zhu, H. Y.; Zhao, J. C.; Zheng, Z. F.; Gao, X. P. Visible-Light-Driven Oxidation of Organic Contaminants in Air with Gold Nanoparticle Catalysts on Oxide Supports. *Angew. Chem., Int. Ed.* **2008**, *47*, 5353-5356.

(8) Fang, J.; Cao, S. W.; Wang, Z.; Shahjamali, M. M.; Loo, S. C. J.; Barber, J.; Xue, C. Mesoporous Plasmonic $Au–TiO_2$ Nanocomposites for Efficient Visible-Light-driven Photocatalytic Water Reduction. *Int. J. Hydrogen Energy* **2012**, *37*, 17853-17861.

(9) Liu, Z.; Sun, D. D.; Guo, P.; Leckie, J. O. An Efficient Bicomponent TiO_2/SnO_2 Nanofiber Photocatalyst Fabricated by Electrospinning with a Side-by-side Dual Spinneret Method. *Nano Lett.* **2007**, *7*, 1081-1085.

(10) Zhang, R.; Wu, H.; Lin, D.; Pan, W. Photocatalytic and Magnetic Properties of the Fe-TiO_2/SnO_2 Nanofiber via Electrospinning. *J. Am. Ceram. Soc.* **2010**, *93*, 605-608.

(11) Cavas, M.; Gupta, R. K.; Al-Ghamdi, A. A.; Serbetci, Z.; Gafer, Z. H.; El-Tantawy, F.; Yakuphanoglu, F. Fabrication and Electrical Characterization of Solution-processed All-oxide Transparent NiO/TiO_2 p-n Junction Diode by Sol-gel Spin Coating Method. *J. Electroceram.* **2013**, *31*, 260-264.

(12) Iwaszyk, A.; Nilan, M.; Jin, Q.; Fujishima, M.; Tada, H. Origin of the Visible-Light Response of Nickel(II) Oxide Cluster Surface Modified Titanium(IV) Dioxide. *J. Phys. Chem. C* 2013, *117*, 2709-2718.

(13) Dalven, R. Physics of Metal–Semiconductor and Metal–Insulator–Semiconductor Junctions, Introduction to Applied Solid State Physics; 2nd ed., Plenum Press: New York-London, 1990, Chapter 4, pp 111–128.

(14) Glassford, K. M.; Chelikowsky, J. R. Electron Transport Properties in RuO_2 Rutile. *Phys. Rev. B: Condens. Matter Mater. Phys.*, **1994**, *49*, 7107-7114.

(15) Hartmann, A. J.; Neilson, M.; Lamb, R. N.; Watanabe, K.; Scott, J. F. Ruthenium Oxide and Strontium Ruthenate Electrodes for Ferroelectric Thin-films Capacitors. A*ppl. Phys. A: Mater. Sci. Process.*, **2000**, *70*, 239-242.

(16) Schafranek, R.; Schaffner, J.; Klein, A. In situ Photoelectron Study of the (Ba,Sr)TiO$_3$/RuO$_2$ Contact Formation. *J. Eur. Ceram. Soc*. **2010,** *30*, 187-192.

(17) Chueh, Y. L.; Hsieh, C. H.; Chang, M .T.; Chou, Li. J. ; Lao, C. S.; Song, J. H.; Gan, J. Y.; Wang, Z. L. RuO$_2$ Nanowires and RuO$_2$/TiO$_2$ Core/Shell Nanowires: From Synthesis to Mechanical, Optical, Electrical, and Photoconductive Properties. *Adv. Mater.* **2007**, *19*, 143-149.

(18) Seitsonen, A. P.; Over, H. Oxidation of HCl over TiO$_2$-Supported RuO$_2$: A Density Functional Theory Study. *J. Phys. Chem. C* **2010**, *114*, 22624-22629.

(19) Ismail, A. A.; Robben, L.; Bahnemann, D. W. Study of the Efficiency of UV and Visible-Light Photocatalytic Oxidation of Methanol on Mesoporous RuO$_2$–TiO$_2$ Nanocomposites. *ChemPhysChem* **2011**, *12*, 982-991.

(20) Kundu, S.; Vidal, A. B.; Yang, F.; Ramirez, P. J.; Senanayake, D. D.; Stacchiola, D.; Evans, J.; Liu, P.; Rodriguez, J. A. Special Chemical Properties of RuO$_x$ Nanowires in RuO$_x$/TiO$_2$(110): Dissociation of Water and Hydrogen Production. *J. Phys. Chem. C* **2012**, *116*, 4767-4773.

(21) Uddin, Md. T.; Nicolas, Y.; Olivier, C.; Toupance, T.; Müller, M. M.; Kleebe, H.-J.; Rachut, K.; Ziegler, J.; Klein, A.; Jaegermann, W. Preparation of RuO$_2$/TiO$_2$ Mesoporous Heterostructures and Rationalization of Their Enhanced Photocatalytic Properties by Band Alignment Investigations. *J. Phys. Chem. C* **2013**, *117,* 22098-22110.

(22) Tebby, Z.; Babot, O.; Toupance, T.; Park, D. H.; Campet, G.; Delville, M. H. Low-temperature UV-Processing of Nanocrystalline Nanoporous Thin TiO$_2$ Films: An Original Route toward Plastic Electrochromic Systems. *Chem. Mater.* **2008**, *20,* 7260-7267.

(23) Cojocaru, L.; Olivier, C.; Toupance, T.; Sellier, E.; Hirsch, L. Size and Shape Fine-Tuning of SnO_2 Nanoparticles for Highly Efficient and Stable Dye-sensitized Solar Cells. *J. Mater. Chem. A*, **2013**, *1*, 13789-13799.

(24) Ensling, D.; Thissen, A.; Gassenbauer, Y.; Klein, A.; Jaegermann, W. In-situ Preparation and Analysis of Functional Oxides. *Adv. Eng. Mater.* **2005,** *7*, 945-949.

(25) Adamski, A.; Spalek, T.; Sojka, Z. Application of EPR Spectroscopy for Elucidation of Vanadium Speciation in VOx/ZrO2 Catalyst Subject to Redox Treatment. *Res. Chem. Intermed.,* **2003**, *29*, 793-804.

(26) Rouquerol, F.; Rouquerol, J.; Sing, K. *Adsorption by Powders & Porous Solids*; Academic Press: New York, 1999, pp 19-20.

(27) Leofanti, G.; Padovan, M.; Tozzola, G ; Venturelli, B. Surface Area and Pore Texture of Catalysts. *Catal. Today*, **1998**, *41*, 207-219.

(28) Qadir, K.; Joo, S. H.; Mun, B. S.; Butcher, D. R.; Renzas, J. R.; Aksoy, F.; Liu, Z.; Somorjai, G. A.; Park, J. Y. Intrinsic Relation between Catalytic Activity of CO Oxidation on Ru Nanoparticles and Ru Oxides Uncovered with Ambient Pressure XPS. *Nanolett.* **2012**, *12*, 5761-5768.

(29) Södergren, S.; Siegbahn, H.; Rensmo, H.; Lindström, H.; Hagfeldt, A.; Lindquist, S.-E. Lithium Intercalation in Nanoporous Anatse TiO_2 Studied with XPS. *J. Phys. Chem. B* **1997**, *101*, 3087-3090.

(30) Guo, Y.; Wang, H.; He, C.; Qiu, L.; Cao, X. Uniform Carbon-Coated ZnO Nanorods: Microwave-Assisted Preparation, Cytotoxicity, and Photocatalytic Activity. *Langmuir* **2009**, *25*, 4678-4684.

(31) Scotti, R.; Bellobono, I. R.; Canevali, C.; Cannas, C.; Catti, M.; D'Arienzo, M.; Musinu, A.; Polizzi, S.; Sommariva, M.; Testino, A.; Morazzoni, F. Sol-Gel Pure and Mixed-Phase Titanium Dioxide for Photocatalytic Purposes: Relations between Phase Composition, Catalytic Activity, and Charge-Trapped Sites. *Chem. Mater.* **2008**, *20*, 4051–4061.

(32) Berger, T.; Diwald, O.; Knozinger, E.; Sterrer, M.; Yates, J. T. UV Induced Local Heating Effects in TiO_2 Nanocrystals. *Phys. Chem. Chem. Phys.* **2006**, *8*, 1822-1826.

(33) Carter, E.; Carley, A. F.; Murphy, D. M. Evidence for O_2^- Radical Stabilization at Surface Oxygen Vacancies on Polycrystalline TiO_2. *J. Phys. Chem. C* **2007**, *111*, 10630-10638

(34) Howe, R. F.; Gratzel, M. EPR Study of Hydrated Anatase under UV Irradiation. *J. Phys. Chem.* **1987**, *91*, 3906-3909.

(35) D'Arienzo, M.; Carbajo, J.; Bahamonde, A.; Crippa, M.; Polizzi, S.; Scotti, R.; Wahba, L.; Morazzoni, F. Photogenerated Defects in Shape-controlled TiO_2 Anatase Nanocrystals: A Probe to Evaluate the Role of Crystal Facets in Photocatalytic Processes. *J. Am. Chem. Soc.* **2011**, *133*, 17652-17661.

(36) Blondeel, G.; Harriman, A.; Porter, G.; Urwin, D.; Kiwi, J. Design, Preparation, and Characterization of RuO_2/TiO_2 Colloidal Catalytic Surfaces Active in Photooxidation of Water. *J. Phys. Chem.* **1983**, *87*, 2629-2636.

(37) Perissinotti, L. L.; Brusa, M. A.; Grela, M. A. Yield of Carboxyl Anion Radicals in the Photocatalytic Degradation of Formate over TiO$_2$ Particles. *Langmuir* **2001,** *17,* 8422-8427.